

# Triple-domain Feature Learning with Frequency-aware Memory Enhancement for Moving Infrared Small Target Detection

Weiwei Duan, Luping Ji\*, *Member, IEEE*, Shengjia Chen, Sicheng Zhu, Mao Ye, *Member, IEEE*

**Abstract**—As a sub-field of object detection, moving infrared small target detection presents significant challenges due to tiny target sizes and low contrast against backgrounds. Currently-existing methods primarily rely on the features extracted only from spatio-temporal domain. Frequency domain has hardly been concerned yet, although it has been widely applied in image processing. To extend feature source domains and enhance feature representation, we propose a new *Triple-domain Strategy* (Tridos) with the frequency-aware memory enhancement on spatio-temporal domain for infrared small target detection. In this scheme, it effectively detaches and enhances frequency features by a local-global frequency-aware module with Fourier transform. Inspired by human visual system, our memory enhancement is designed to capture the spatial relations of infrared targets among video frames. Furthermore, it encodes temporal dynamics motion features via differential learning and residual enhancing. Additionally, we further design a residual compensation to reconcile possible cross-domain feature mismatches. To our best knowledge, proposed Tridos is the first work to explore infrared target feature learning comprehensively in spatio-temporal-frequency domains. The extensive experiments on three datasets (i.e., DAUB, ITSdT-15K and IRDST) validate that our triple-domain infrared feature learning scheme could often be obviously superior to state-of-the-art ones. Source codes are available at <https://github.com/UESTC-nnLab/Tridos>.

**Index Terms**—Moving Infrared Small Target Detection, Triple-domain Feature Learning, Fourier Transform, Frequency Aware, Memory Enhancement

## I. INTRODUCTION

**I**NFRARED small target detection (ISTD) has the advantages of being less negatively affected by the environment and being highly resistant to external electromagnetic interference [48]. It holds significant application value in some military and civil fields, such as early invasion warning, infrared guidance and maritime rescue [47]. Although ISTD has been developing rapidly in recent years, it still faces huge challenges. First, due to their tiny size, infrared targets could often lack some obvious visual features, such as shapes and textures. Second, with a large detection range, targets are often characterized by low contrast and low signal-to-noise ratio (SNR). Third, the fast motion of targets and background

\*Corresponding author: Luping Ji.

This work is supported by the Aeronautical Science Foundation of China (ASFC) under Grant No. 2022Z071080006 and the National Natural Science Foundation of China (NSFC) under Grant No. 61972072.

Weiwei Duan, Luping Ji, Shengjia Chen, Sicheng Zhu and Mao Ye are with the School of Computer Science and Engineering, University of Electronic Science and Technology of China, Chengdu 611731, China (e-mail: dww@std.uestc.edu.cn; jiluping@uestc.edu.cn; shengjia-chen@std.uestc.edu.cn; sichengzhu@std.uestc.edu.cn; maoye@uestc.edu.cn)

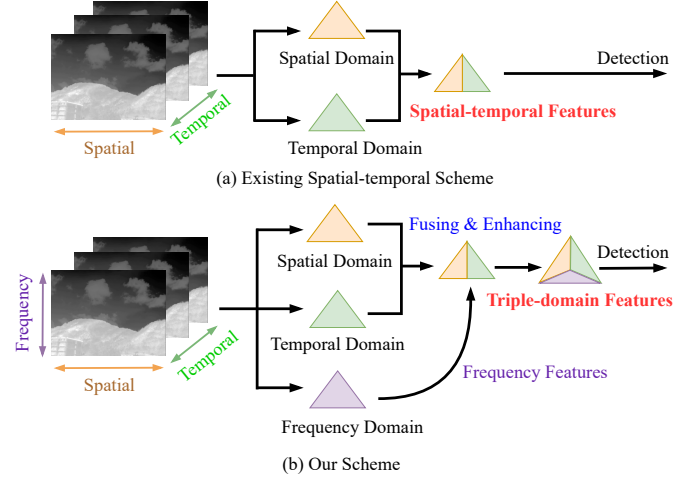


Fig. 1: The comparison between existing spatio-temporal scheme and our triple-domain learning scheme. Our scheme extracts features in spatio-temporal-frequency domains.

noise interference usually result in severe infrared background fluctuations, and target boundary blurring. Consequently, accurately locating and tracking moving small targets in infrared images and videos has been an attractive research area in computer vision, full of research challenging.

Over the past decades, many detection approaches have been proposed. From the difference of research strategies, they could usually be categorized into model-driven and data-driven methods [16]. Model-driven methods deeply analyze image characteristics to distinguish targets from backgrounds, often by contrast and texture differences [1], [3]. Although these methods have achieved impressive results, they heavily depend on prior knowledge and hand-crafted features, lacking learning ability [24]. Recently, artificial intelligence technologies, especially deep learning, have been developing rapidly, e.g., the SpectralGPT [61], LRR-Net [62] and CasFormer [63]. These methods show impressive promise, due to their efficient capabilities of feature learning. Currently, data-driven methods, which are mainly based on deep learning [9], [14], [15], have become the mainstream schemes to learn feature representations and target detection inference from labeled dataset samples [52].

Furthermore, according to the difference of image-frame numbers, existing detection methods could be further divided into single-frame and multi-frame schemes [29]. Generally,

single-frame ISTD (SISTD) methods, e.g., DNANet [12], RISTD [43] and RPCANet [19], extract target features only from spatial domain, often with obvious advantages of low complexity and high detection speed. In contrast, multi-frame ISTD (MISTD) methods could further improve detection performance. This improvement is attributed to that these methods, e.g., STDManet [30], ST-Trans [57] and SSTNet [32], can extract more discriminative target features from both spatial and temporal domains, as shown in Fig. 1(a).

Currently, almost all MISTD methods [30], [57], [32] are only based on spatio-temporal features. This type of approaches could achieve good detection performance. Nevertheless, they often fail to sufficiently capture the intricate characteristics of moving small targets. Besides, some targets in complex backgrounds could usually not exhibit a high correlation in consecutive frames. These limitations above make it challenging to precisely discern infrared target motion details and contours, ultimately decreasing detection performance. Generally, the information from different domains is complementary [2]. This could help to characterize infrared small target features more comprehensively. Therefore, our initial motivation is to introduce more information domains for infrared feature learning, further strengthening infrared small target detection paradigm.

Many image processing studies, such as [51] and [50], have proved that frequency domain features can provide abundant frequencies information. Meanwhile, more researches have demonstrated that frequency information is significantly practical in image feature modeling, e.g., DAWN [58], FMRNet [59] and frequency-assisted mamba [60]. Besides, observed in frequency domain, noise usually distributes at high frequencies, while targets distribute at low frequencies [3]. Based on these findings, frequency information is believed to be potentially valuable in infrared small target detection.

To further enhance infrared target feature learning, on traditional spatio-temporal domains, we propose a new *Triple-domain Strategy* (Tridos) with frequency-aware memory enhancement, as shown in Fig. 1(b). Our scheme is dedicated to exploiting the potential of frequency information and enhancing infrared target representation comprehensively. In details, our work focuses on depicting infrared targets simultaneously in spatio-temporal-frequency domains, specially leveraging their dynamic variations in frequency domain to promote target detection performance. Our Tridos is not a simple fusion of frequency and spatio-temporal feature learning. By contrast, it captures frequency features and then enhances spatio-temporal features using frequency features, even concerning cross-domain mismatches. It is believed to be the first work to model the MISTD task from a frequency-aware spatio-temporal perspective. In summary, the main contributions of our work are summarized as follows:

(I) We explore and propose Tridos, a pioneering triple-domain scheme to extend the feature learning perspective for MISTD. In addition to traditional spatio-temporal domains, it can capture target features from frequency domain and then realize the fusion and enhancement of spatio-temporal-frequency features.

(II) Based on Fourier transform, a local-global frequency-

aware module is developed to extract comprehensive frequency features from local and global perceptual patterns. Additionally, inspired by human visual system, a memory-enhanced spatial relationship module is designed to model the inter-frame correlations of small targets.

(III) A residual compensation unit is constructed to eliminate the possible feature mismatches between different domains, and then auxiliarily fuse & enhance spatio-temporal-frequency features of small targets.

(IV) A new dual-view regression loss function is re-defined to optimize model training, especially tailored for ISTD.

## II. RELATED WORK

### A. Single-frame Infrared Small Target Detection

Single-frame infrared small target detection deals with stationary targets in a single image. It can often be divided into model-driven and data-driven methods.

Model-driven methods detect small targets by exploiting image characteristics for target enhancement or background suppression, often with threshold segmentation [53]. This types of methods can be further categorized into filter-based, human visual system (HVS)-based, and data structure-based methods. Filter-based methods utilize the difference between target and background pixels to highlight targets and remove background noise interference, e.g., Top-hat [1] and Maxmean [2]. HVS-based methods extract salient regions by measuring the maximum contrast between center pixel and its neighboring regions, e.g., local contrast measure (LCM) [3] and its modified versions: RLCM [4], HBMLCM [5] and WSLCM [6]. Data structure-based methods employ the special structure of infrared images to separate targets from background, e.g., SMSL [8]. Although these model-driven approaches have achieved outstanding performance, they could often not adapt to intricate environments.

In contrast, data-driven methods primarily exploit deep neural networks that can adaptively learn target features by the training on numerous labeled samples. These ones have become dominant, with the availability of infrared small target detection datasets [9], [12], [10]. For example, ACMNet [9] integrates low-level details and high-level semantics through asymmetric contextual modulation, and it further introduces dilated local contrast measurements in ALCNet [13]. DNANet [12] designs a dense nested interactive network to enhance the features of small targets. Moreover, AGPCNet [14] develops an attention-guided pyramid context network to obtain a global association of semantics. RDIAN [15] uses multi-scale convolutions to capture diverse target features and extend receptive fields. UIUNet [17] integrates two U-nets to learn multi-scale and multi-level feature representations. ISNet [10] creatively emphasizes the importance of target shapes. Furthermore, EFLNet [18] constructs a feature-enhancing learning network, and RPCANet [19] proposes an interpretable deep neural network with theory-guided to replace matrix computation.

Totally, single-frame infrared small target detection has been widely studied and has performed well. However, this type of pipeline cannot always utilize target motion features. It is susceptible to noise and background interference, especially in challenging detection scenarios.

## B. Multi-frame Infrared Small Target Detection

In contrast, multi-frame detection schemes usually process multiple consecutive frames simultaneously. Therefore, how to extract the spatio-temporal features of targets has received extensive attention.

In representative traditional schemes, optical flow-based methods [21], [20] utilize the brightness variations in different frames to describe target motion features. STCP [21] employs optical flow algorithm to compute the dense trajectory of targets, then it creates a binary image to extract salient contours as candidate target regions. Some methods construct spatio-temporal tensors to distinguish targets from backgrounds, such as 4D STT [22] and NPSTT [24]. To solve the issue of inaccurate background estimation, NTLA [25] proposes a nonconvex tensor low-order approximation strategy. FST-FLNN [23] improves tensor nuclear norm by log operation for target enhancement and background suppression. Moreover, energy accumulation-based methods [26], [27] can effectively improve SNR and enhance the energy of small targets. Dynamic programming-based methods [28] search for the optimal motion trajectory of targets usually through dynamic programming algorithm. Although these traditional methods have made some progress, they rely on prior knowledge heavily.

To overcome the problems appearing in traditional methods, some new approaches apply deep learning to MISTD. This type of pipeline can exploit the temporal association between sequential frames to improve target detection performance. However, it remains largely unexplored due to the lack of adequate MISTD datasets with high-quality annotations. In recent years, some representative methods have been proposed. For example, the inter-frame energy accumulation enhancement is proposed in [29]. STDMA Net [30] introduces a spatio-temporal differential multiscale attention network, a pioneering study with temporal attention mechanism. DTUM [31] is designed to encode motion direction and extract target motion information. Moreover, SSTNet [32] devises a sliced spatio-temporal network to employ cross-slice motion context. Recently, ST-Trans [33] introduces a spatio-temporal transformer to learn inter-frame associations and handle complex detection scenarios. However, these methods solely focus on effectively extracting and utilizing target features only from spatio-temporal domains, neglecting the utilization of frequency information implied in consecutive frames.

Therefore, in this work, we focus on introducing frequency-domain information to expand target feature learning. For intuitiveness and clarity, we summarize the typical differences between our Tridos and related works, as follows:

(I) Triple-Domain Feature Learning: existing works focus on feature learning from spatio-temporal domains. In contrast, our method leverages additional frequency domain features to refine the detection paradigm.

(II) Inter-Frame Relation Mining: previous methods usually compute the weights of each frame, and only consider simple inter-frame relationships. Different from them, our method mimics human memory mechanisms to capture the global dependencies of targets in different time steps.

(III) Cross-Domain Feature Reconciling: unlike existing works that use some classic operations such as convolution and concatenation for feature fusion, we use residual compensation to ameliorate cross-domain feature collaboration.

## III. METHODOLOGY

### A. Overall Architecture

We aim to effectively promote the detection performance of MISTD by triple-domain feature learning. A new framework is proposed to fulfill this goal, as presented in Fig. 2. For clarity, its simplified workflow is shown in Fig. 3.

In our framework, it randomly sample a collection of consecutive frames  $\mathbf{I}_c = \{\mathbf{I}_1, \mathbf{I}_2, \dots, \mathbf{I}_t\}$  from an infrared video with time window size of  $T = t$  as input.  $\mathbf{I}_t$  is the keyframe that needs to be detected, and the other ones are reference frames used for providing context information. Then, we feed each frame into the feature extractors with shared weights to obtain multi-frame features  $\mathbf{F}_c = \{\mathbf{F}_1, \mathbf{F}_2, \dots, \mathbf{F}_t\} \in \mathbb{R}^{T \times C \times H \times W}$ , where  $C$ ,  $H$  and  $W$  indicate the channel, height and width of feature matrix, respectively. Specifically, we adopt the CSPDarknet [35] as backbone. We design three branches to realize the strategy of triple-domain feature learning through memory-enhanced spatial relationship module (MSRM), temporal dynamic encoding module (TDEM), and local-global frequency-aware module (LGFM). The residual compensation unit (RCU) then aims to eliminate the potential feature mismatches across different domains while fusing and enhancing different domain features. Afterwards, the adequately interacted spatio-temporal-frequency features,  $\mathbf{F}_{stf}$  are delivered to a detection head to obtain final detection results.

MSRM receives multi-frame features  $\mathbf{F}_c$  as its input and generates the memory-enhanced spatial features  $\mathbf{F}_S$ . Similarly, we introduce TDEM to extract target motion features  $\mathbf{F}_T$  by employing differential learning and residual enhancing between neighboring frames. To incorporate both the location and motion information of targets, we concatenate spatial features  $\mathbf{F}_S$  and temporal features  $\mathbf{F}_T$  to form spatio-temporal features  $\mathbf{F}_{st}$ , as follows:

$$\mathbf{F}_{st} = \text{Conv}(\text{Concat}[\mathbf{F}_S, \mathbf{F}_T]) \quad (1)$$

where  $\text{Conv}$  denotes a  $3 \times 3$  convolutional layer, with batch normalization and SiLU activation function. Inspired by Fourier Transform, we transform multi-frame features  $\mathbf{F}_c$  into frequency domain. LGFM is proposed for modeling the local-global variation of targets in frequency domain, enhancing target representation from different perspectives.

$$\mathbf{F}_{lf}, \mathbf{F}_{gf} = \text{LGFM}(\mathbf{F}_c) \quad (2)$$

where  $\mathbf{F}_{lf}$  and  $\mathbf{F}_{gf}$  indicate the local and global features in frequency domain, respectively. Then,  $\mathbf{F}_{lf}$ ,  $\mathbf{F}_{gf}$  and  $\mathbf{F}_{st}$  are fed into the designed RCUs to facilitate feature interaction and alleviate the feature mismatches in different domains. Their calculation processes are as follows:

$$\begin{cases} \mathbf{F}_{stf_1} = \text{RCU}_1(\mathbf{F}_{lf}, \mathbf{F}_{st}) \\ \mathbf{F}_{stf_2} = \text{RCU}_2(\mathbf{F}_{gf}, \mathbf{F}_{st}) \end{cases} \quad (3)$$

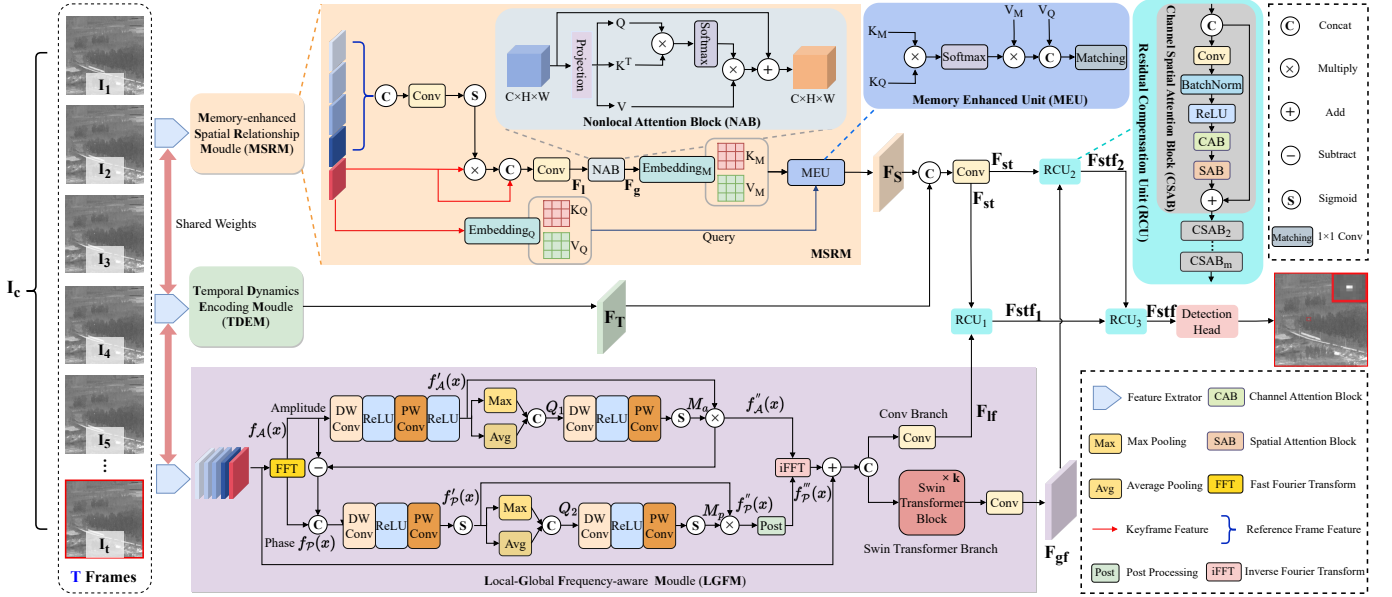


Fig. 2: Overview of proposed framework Tridos.  $\mathbf{I}_c$  is a group of video frames for Tridos. It consists of a backbone and three primary branches, i.e., a *Memory-enhanced Spatial Relationship* extraction branch, a *Temporal Dynamic Encoding* branch, and a *Local-Global Frequency-aware* branch. The features extracted by the first two branches are fused together to generate  $\mathbf{F}_{st}$ . The two outputs of the third branch,  $\mathbf{F}_{lf}$  and  $\mathbf{F}_{gf}$  are fused with  $\mathbf{F}_{st}$  by RCU to generate  $\mathbf{F}_{stf_1}$  and  $\mathbf{F}_{stf_2}$ , respectively. Finally,  $\mathbf{F}_{stf_1}$  and  $\mathbf{F}_{stf_2}$  are further compensated by RCU to obtain the refined features  $\mathbf{F}_{st}$  for designed detection head.

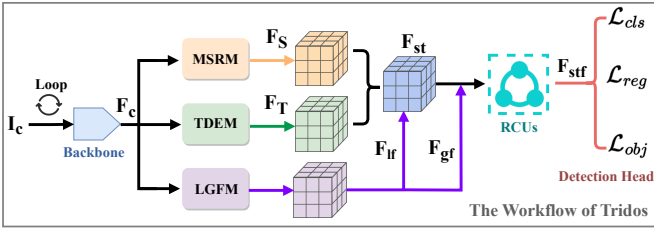


Fig. 3: The workflow of Tridos. It contains the calculation process of input  $\mathbf{I}_c$  and the feature flow of target detection.

After that, we can obtain the compensated spatio-temporal-frequency features  $\mathbf{F}_{stf} = RCU_3(\mathbf{F}_{stf_1}, \mathbf{F}_{stf_2})$ . Finally, infrared target detection results are acquired by the decoupled head of YOLOX [35] and non-maximal suppression.

### B. Memory-enhanced Spatial Relationship Module

Spatial relationship modeling is crucial for accurately predicting and tracking target locations. Previous methods directly combine multi-frame spatial features via concatenation [29] or multi-layer convolution [30]. However, these ones seldom consider the keyframe's global context information and the spatial dependencies between neighboring frames. To address this, we propose MSRM, as shown in Fig. 2. In it, non-local attention block (NAB) is introduced to capture the long-distance dependencies between pixels in different time steps. When tracking moving targets, humans can recognize targets more accurately and extract target's spatial relationships by comparing and inferring the features between a keyframe and its reference frames. Therefore, inspired by human visual

system, we devise the memory enhancement unit (MEU) to expand target features. It could fully employ multi-frame features by creating key-value pairs to better capture the spatial relationships between targets.

Specifically, in MSRM, we first merge the features of reference frames and keyframe through following computational process. We assign different weights to different pixels in reference frames.

$$\hat{\mathbf{F}}_t = \sigma(\text{Conv}(\text{Concat}[\mathbf{F}_1, \dots, \mathbf{F}_{t-1}])) \otimes \mathbf{F}_t \quad (4)$$

$$\mathbf{F}_l = \text{Conv}(\text{Concat}[\hat{\mathbf{F}}_t, \mathbf{F}_t])$$

where  $\sigma$  denotes a Sigmoid function,  $\otimes$  is element-wise multiplication,  $\hat{\mathbf{F}}_t$  denotes updated keyframe feature, and  $\mathbf{F}_l$  indicates local inter-frame spatial relations.

Then, we send  $\mathbf{F}_l$  to NAB to explore the correlation between different pixels across frames, overcoming the local limitations of convolutional layers, as follows:

$$\mathbf{Q}, \mathbf{K}, \mathbf{V} = \text{Projection}(\mathbf{F}_l)$$

$$\mathbf{F}_g = \gamma \cdot \text{Softmax}\left(\frac{\mathbf{Q}\mathbf{K}^T}{\sqrt{d}}\right)\mathbf{V} + \mathbf{F}_l \quad (5)$$

where  $\text{Projection}(\cdot)$  is a linear transform implemented by  $1 \times 1$  convolution,  $\gamma$  is a hyper-parameter,  $\sqrt{d}$  is the scale factor for normalization, and  $\mathbf{F}_g$  denotes inter-frame local-global spatial relations. In this way, any two pixels can interact and be captured long-distance dependencies, not just being limited to local neighboring pixels.

After that, we store the local-global spatial features  $\mathbf{F}_g$  in memory and the keyframe features  $\mathbf{F}_t$  as query, similar to the visual tracking mechanism of human brain. In detail, we em-

ploy four distinct embedding layers to generate corresponding key-value pairs, as follows.

$$\begin{cases} \mathbf{K}_Q, \mathbf{V}_Q = f_Q(\mathbf{F}_t) \\ \mathbf{K}_M, \mathbf{V}_M = f_M(\mathbf{F}_g) \end{cases} \quad (6)$$

where  $f_Q(\cdot)$  and  $f_M(\cdot)$  represent different embedding layers.  $K$  is utilized to align the location information of targets, and  $V$  holds the high-level semantic features of targets. In MEU, we first calculate the similarity between  $\mathbf{K}_M$  and  $\mathbf{K}_Q$ , with *Softmax* normalizing. Subsequently, the regions related to target features are queried from  $\mathbf{V}_M$  and then concatenated with  $\mathbf{V}_Q$ . This establishes the connection between keyframe and its reference frames, leading to the improvement of target features with the visual information from memory. MEU is computed mathematically as follows:

$$\begin{aligned} M_s &= \text{Softmax}(\mathbf{K}_M \otimes \mathbf{K}_Q) \\ F_S &= \text{Matching}(\text{Concat}[M_s \otimes \mathbf{V}_M, \mathbf{V}_Q]) \end{aligned} \quad (7)$$

where  $M_s$  is the similarity matrix of  $\mathbf{K}_M$  and  $\mathbf{K}_Q$ , *Matching* represents  $1 \times 1$  convolution, and  $F_S$  denotes the local-global spatial features by memory enhancement.

### C. Temporal Dynamics Encoding Module

How to extract the motion paradigm of targets is a challenging problem in MISTD. Previous methods often use optical flow [20] or recurrent neural networks [32]. However, since targets are too small, the motion information between neighboring frames is not obvious, making the extraction of motion features challenging. Recently, temporal difference learning has emerged as an effective paradigm for extracting motion information from video sequences, as in LGTD [55] and TDN [54]. These works lay the foundation for utilizing temporal difference learning in various applications. Inspired by these, we design a TDEM, as shown in Fig. 4. It stacks all adjacent frames' differential information within time window to solve the sparsity issue observed in a single difference. Unlike previous methods, we also incorporate residual blocks to amplify small targets' motion features through enhancing differential information. In detail, TDEM dynamically encodes difference maps and propagates local motions into keyframe features. As shown in Fig. 4, we set the size of time window to  $T = 5$ . Initially, we acquire continuous local motions  $\mathbf{D} = [d_1, d_2, d_3, d_4]$  in sequential images by subtracting adjacent frames. Then, we use a  $3 \times 3$  convolution and downsample through an average pooling with a stride of 2 to extract the motion dependencies of targets  $\mathbf{F}_D$ . This step can be expressed as follows:

$$\mathbf{F}_D = \text{Avg}(\text{Conv}(\text{Stack}(d_1, d_2, d_3, d_4))) \quad (8)$$

where *Avg* means average pooling and *Stack* represents a splice operation on dimension 1. Downsampling is executed due to two main considerations. One is that differential information is sparse, and motions are more prominent in low-resolution space. The other is that pooling can reduce the computational cost of temporal dynamic encoding.

Moreover, we integrate both motion and keyframe features to cope with the dynamic changes of targets in temporal

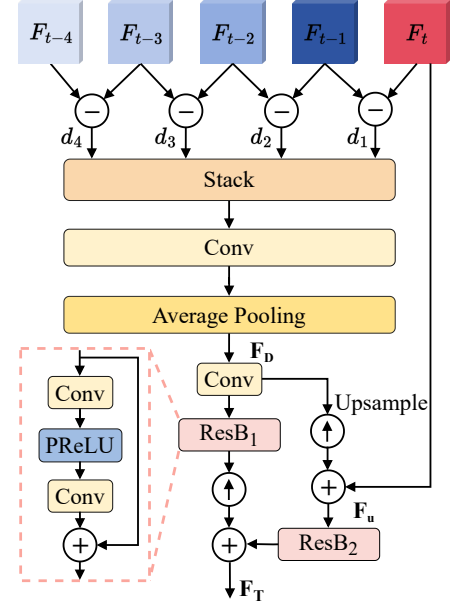


Fig. 4: The details of our proposed TDEM, with time window  $T = 5$ . ResB<sub>1</sub> and ResB<sub>2</sub> are two residual blocks for enhancing differential information.

dimension. The motion dependencies,  $\mathbf{F}_D$  are restored as its original size and then added to keyframe features. Furthermore, we utilize two residual blocks to enhance local motion, and deeply incorporate motion dependencies and target features. They can be calculated as follows:

$$\begin{aligned} \mathbf{F}_u &= \mathbf{F}_t + f_u(\text{Conv}(\mathbf{F}_D)) \\ \mathbf{F}_T &= \text{ResB}_2(\mathbf{F}_u) + f_u(\text{ResB}_1(\text{Conv}(\mathbf{F}_D))) \end{aligned} \quad (9)$$

where  $f_u$  is an upsample operation, and  $\mathbf{F}_T$  denotes the motion features obtained by temporal dynamic encoding. *ResB* represents the residual block which consists of two  $3 \times 3$  convolutions and a PReLU activation function.

### D. Local-global Frequency-aware Module

Frequency domain features provide a comprehensive understanding to infrared small targets at various frequencies, while also reducing image noise and interference. Our objective is to thoroughly explore the potential of frequency for expanding target feature learning.

As shown in Fig. 2, designed LGFM has two branches dedicated to modeling and extracting frequency features from multiple views and levels. One is the convolution branch, which captures local correlations and spatial structures from frequency. The other is the Swin Transformer [38] branch, which globally models and encodes frequency features using a sliding window mechanism. This branch improves the receptive field, allowing for extracting global contexts.

Concretely, the Fourier transform [37]  $f_{\mathcal{F}}(\cdot)$  converts each frame's features into frequency domain. Simply, for given features  $x$ , this process can be formulated as follows :

$$f_{\mathcal{F}}(x)(u, v) = \sum_{h=0}^{H-1} \sum_{w=0}^{W-1} x(h, w) e^{-j2\pi(\frac{h}{H}u + \frac{w}{W}v)} \quad (10)$$

where  $u$  and  $v$  represent the horizontal and vertical components of frequency.  $H$  and  $W$  are the height and width of given  $x$ . The frequency domain information,  $f_{\mathcal{F}}(x)$  can be further decomposed into amplitude  $f_{\mathcal{A}}(x)$  and phase  $f_{\mathcal{P}}(x)$ , by

$$\begin{cases} f_{\mathcal{A}}(x)(u, v) = [\mathcal{R}^2(x)(u, v) + \mathcal{I}^2(x)(u, v)]^{1/2} \\ f_{\mathcal{P}}(x)(u, v) = \arctan \left[ \frac{\mathcal{I}(x)(u, v)}{\mathcal{R}(x)(u, v)} \right] \end{cases} \quad (11)$$

where  $\mathcal{R}(x)$  and  $\mathcal{I}(x)$  represent the real and imaginary part of  $f_{\mathcal{F}}(x)$ , respectively.

The motivation for decomposing frequency features into amplitude and phase is to employ the information from these two aspects. Amplitude reflects the feature energy distribution of different frequencies, while phase comprises the position and relative relationship in frequency domain. Initially, we process amplitude and then utilize amplitude residuals to further extract and refine phases. To achieve this, we use a  $3 \times 3$  depth-wise convolution, i.e.,  $DW(\cdot)$ , to independently learn spatial context information on each channel, and a cross-channel blending with  $1 \times 1$  point-wise convolution, i.e.,  $PW(\cdot)$ , to aggregate pixels, as follows:

$$f'_{\mathcal{A}}(x) = ReLU(PW(ReLU(DW(f_{\mathcal{A}}(x))))) \quad (12)$$

To enhance the energy of moving infrared small targets, we apply max pooling  $Max(\cdot)$  and average pooling  $Avg(\cdot)$  along channel dimension and then concatenate them. We apply the similar transformation on  $f'_{\mathcal{A}}(x)$  to get the amplitude attention map  $M_{\mathbf{a}}$ . Then,  $M_{\mathbf{a}}$  multiplies with  $f'_{\mathcal{A}}(x)$  to get the final refined amplitude features  $f''_{\mathcal{A}}(x)$ , which can be formulated as follows:

$$\begin{cases} \mathbf{Q}_1 = Concat[Avg(f'_{\mathcal{A}}(x)), Max(f'_{\mathcal{A}}(x))] \\ M_{\mathbf{a}} = \sigma(PW(ReLU(DW(\mathbf{Q}_1)))) \\ f''_{\mathcal{A}}(x) = f'_{\mathcal{A}}(x) \otimes M_{\mathbf{a}} \end{cases} \quad (13)$$

where  $\mathbf{Q}_1 \in \mathbb{R}^{2 \times H \times W}$  and  $\sigma$  is a *Sigmoid* function.

After that, we employ amplitude residuals  $f_{\mathcal{R}}(x) = f''_{\mathcal{A}}(x) - f_{\mathcal{A}}(x)$ , which contain subtle amplitude variations to modify input and guide phase features extraction. Regarding phases, we follow a similar procedure to amplitudes, by

$$\begin{cases} f'_{\mathcal{P}}(x) = \sigma(PW(ReLU(DW(Concat[f_{\mathcal{P}}(x), f_{\mathcal{R}}(x)])))) \\ \mathbf{Q}_2 = Concat[Avg(f'_{\mathcal{P}}(x)), Max(f'_{\mathcal{P}}(x))] \\ M_{\mathbf{p}} = \sigma(PW(ReLU(DW(\mathbf{Q}_2)))) \\ f''_{\mathcal{P}}(x) = f'_{\mathcal{P}}(x) \otimes M_{\mathbf{p}} \end{cases} \quad (14)$$

Moreover, we apply post-processing to restrict the phase values to  $[-\pi, \pi]$ , which maintains the continuity and stability of phases. For combining amplitude and phase, we employ the  $Cos(\cdot)$  and  $Sin(\cdot)$  functions to compute the real and imaginary components of features, as follows:

$$\begin{cases} f'''_{\mathcal{P}}(x) = 2\pi \cdot f''_{\mathcal{P}}(x) - \pi \\ \mathcal{R}'(x)(u, v) = f''_{\mathcal{A}}(x)(u, v) \cdot Cos(f'''_{\mathcal{P}}(x)(u, v)) \\ \mathcal{I}'(x)(u, v) = f''_{\mathcal{A}}(x)(u, v) \cdot Sin(f'''_{\mathcal{P}}(x)(u, v)) \end{cases} \quad (15)$$

where  $x'_{\mathcal{F}} = \mathcal{R}'(x) + \mathcal{I}'(x)j$  indicates integrated frequency features. Then, the inverse Fourier transformation  $f_{\mathcal{F}}^{-1}(\cdot)$  is

used to transform  $x'_{\mathcal{F}}$  back to its original domain. Suppose the input feature is  $x$ , its final output  $x'$  is obtained by adding  $x$  and its transformed features through residuals, by:

$$x' = x + f_{\mathcal{F}}^{-1}(x'_{\mathcal{F}}) \quad (16)$$

For the input of multi-frame feature collection  $F_c$ , we process each frame separately to obtain outputs  $F'_c = \{F'_1, F'_2, \dots, F'_t\} \in \mathbb{R}^{T \times C \times H \times W}$ . Finally, we splice them to feed into two separate branches, as follows:

$$\begin{aligned} F_{lf} &= ConvB(Concat[F'_1, F'_2, \dots, F'_t]) \\ F_{gf} &= SwinB(Concat[F'_1, F'_2, \dots, F'_t]) \end{aligned} \quad (17)$$

where  $F_{lf}$  is the local frequency features from convolution branch  $ConvB(\cdot)$ . This branch contains two  $3 \times 3$  convolution layers with stride 1, batch normalization and SiLU activation function.  $F_{gf}$  denotes the global frequency features, acquired from a Swin Transformer branch, i.e.,  $SwinB(\cdot)$ .

### E. Residual Compensation Unit

Our scheme thoroughly explores the spatial, temporal and frequency domain features of infrared targets. However, feature mismatches could often happen due to the learning path differences of different domain features. Therefore, we need to further compensate features to retain valuable information in all triple domains. With the help of RCU, the differences and commonalities between different-domain features can be fused and enhanced. This step helps to strengthen the understanding to samples, and reduce the sensitivity to interference.

As shown in Fig. 2, our RCU comprises several channel spatial attention blocks (CSAB). For example, for local frequency features  $F_{lf}$  and spatio-temporal features  $F_{st}$ , we first splice them along channel dimension and use a  $3 \times 3$  convolution also followed by batch normalization and ReLU (denoted as  $Conv$ ) to further enhance target features. Then, we introduce a channel attention block (CAB) and a spatial attention block (SAB) to weight the features from different channels and spatial locations, adaptively focusing on target significant information. Furthermore, feature compensation is performed by a residual branch. The residual compensation between  $F_{lf}$  and  $F_{st}$ ,  $F_{stf_1}$  can be computed by

$$\begin{cases} F_r = Concat[F_{lf}, F_{st}] \\ CSAB = f_{SAB}(f_{CAB}(Conv(F_r))) + F_r \\ F_{stf_1} = CASB_m(CASB_{m-1}(\dots CASB_1(F_r))) \end{cases} \quad (18)$$

where  $m$  is the number of CSAB. Similarly, on  $F_{gf}$  and  $F_{st}$ , we perform the same operations as on  $F_{lf}$  and  $F_{st}$  to obtain  $F_{stf_2}$ . Also similarly, on both  $F_{stf_1}$  and  $F_{stf_2}$ , final infrared small target feature refinement  $F_{stf}$  is generated.

### F. Dual View Regression Loss

Following a general paradigm of detection [14], a traditional loss function can be expressed as

$$\mathcal{L} = \lambda_{reg} \mathcal{L}_{reg} + \lambda_{cls} \mathcal{L}_{cls} + \lambda_{obj} \mathcal{L}_{obj} \quad (19)$$

where  $\mathcal{L}_{reg}$  is a bounding box regression loss, usually calculated by IoU loss.  $\mathcal{L}_{cls}$  is a classification loss and  $\mathcal{L}_{obj}$  is a

target probability loss.  $\lambda_{reg}$ ,  $\lambda_{cls}$  and  $\lambda_{obj}$  are three hyper-parameters to balance loss terms.

For traditional  $\mathcal{L}_{cls}$  and  $\mathcal{L}_{obj}$ , we employ sigmoid focal loss [39] to solve the problem of positive and negative sampling imbalance. Due to small target size, popular IoU loss could be insufficient to capture the detailed information of target distribution. Considering this, a normalized Gaussian Wasserstein distance (NWD) loss [40] can be adopted to minimize the difference between target boxes by introducing Gaussian distribution. It could efficiently model the target boxes of different sizes and positions.

IoU loss assists our network to accurately localize small targets, while NWD loss learns their distributional properties. Therefore, we design a new  $\mathcal{L}_{dvr}$  on IoU and NWD losses to further enhance traditional  $\mathcal{L}_{reg}$ , as follows:

$$\begin{cases} \mathcal{L}_{iou} = 1 - IoU(B_P, B_G) \\ \mathcal{L}_{nwd} = 1 - \exp(-\frac{\sqrt{\|N_P, N_G\|_2^2}}{C}) \\ \mathcal{L}_{reg} = \mathcal{L}_{dvr} = \alpha \mathcal{L}_{iou} + \beta \mathcal{L}_{nwd} \end{cases} \quad (20)$$

where  $B_P$  is a predicted bounding box, while  $B_G$  is a labeled box.  $N_P$  and  $N_G$  denote the Gaussian distribution of predicted boxes and that of labeled boxes, respectively.  $C$  is a constant related to datasets. Coefficients  $\alpha$  and  $\beta$  are two hyper-parameters to balance loss terms.

## IV. EXPERIMENTS

### A. Datasets and Evaluation Metrics

Usually, dataset quality, sample quantity and scenario diversity could significantly impact the detection performance of data-driven methods. Currently, there are a few datasets [15], [42] for MISTD. These ones are intended for aerial-based applications and aim at airborne, not for ground-based vehicle targets. Thus, we re-organize an additional MISTD dataset on this public repository [34], i.e., ITSDT-15K, to extend the quality, quantity and diversity of infrared multi-frame datasets. The dim-small targets in these images are moving vehicles captured by UAV infrared cameras. For ITSDT-15K, we have removed all wrong image sequences and revised all labeled bounding boxes to ensure that they accurately represent infrared targets. Then, we randomly selected 15K images, and split them into the 10K training images of 40 videos and the 5K test images of 20 videos. Besides, all frame-images have the same resolution of  $640 \times 480$ .

New ITSDT-15K dataset contains a variety of complex scenarios, including grass, forests, obstacles, and ground clutter. Overall, our ITSDT-15K is adequate for evaluating the performance of different methods for MISTD. Accordingly, we employ ITSDT-15K and two public datasets, DAUB [42] and IRDST [15], for method evaluation in experiments. All compared methods are evaluated on the revised ITSDT-15K dataset, as fair as possible. On DAUB and IRDST, we follow [32] to divide their training sets and test sets.

In terms of evaluation metrics, following the common practice of target detection paradigm, we apply Precision (%), Recall (%), F1 score (%), and *Average Precision* (%) (e.g.,

TABLE I: The parameter settings for model-driven methods.

Method	Parameters
MaxMedian [2]	filter size: 5
TopHat [1]	structure size: $5 \times 5$
RLCM [4]	scale = 3, $k1 = [2, 5, 9]$ , $k2 = [4, 9, 16]$
HBMLCM [5]	scale size: [3, 5, 7, 9], external window size: $15 \times 15$
PSTNN [24]	patch size: 40, slide step: 40, $\lambda_L = 0.7$
WSLCM [6]	gaussian kernel: $\frac{1}{16} \begin{bmatrix} 1 & 2 & 1 \\ 2 & 4 & 2 \\ 1 & 2 & 1 \end{bmatrix}$ , scale size: [3, 5, 7, 9]

mAP<sub>50</sub>, the average Precision with an IOU threshold 0.5). These metrics can be formulated by

$$\begin{aligned} \text{Precision} &= \frac{TP}{TP + FP} \\ \text{Recall} &= \frac{TP}{TP + FN} \\ \text{F1} &= \frac{2 \times \text{Precision} \times \text{Recall}}{\text{Precision} + \text{Recall}} \end{aligned} \quad (21)$$

where TP, FP and FN denote the number of correct detection targets (True positive), false alarms (False positive) and missed detection targets (False negative), respectively. As a comprehensive metric to assess detection methods, F1 score is computed by combining both Precision and Recall.

### B. Implementation Details

In implementation, time window size  $T$  is set to 5. For all methods, we reshape the resolution of infrared frames to  $512 \times 512$ , as fair as possible. We train our Tridos for 100 epochs with batch size 4. Initial learning rate is 0.001 and decreased adaptively with training epochs. Adam is employed as an optimizer with a CosineAnnealingLR scheduler and momentum 0.937. We initialize model weights with a usual distribution. For hyper-parameters, we set  $\lambda_{reg}$ ,  $\lambda_{cls}$  and  $\lambda_{obj}$  in Eq. (19) to 5, 1 and 1, respectively. The  $\alpha$  and  $\beta$  in Eq. (20) are both 0.5. During model testing, the IoU threshold for non-maximum suppression is always 0.65, and only the predicted boxes with a confidence greater than 0.001 are retained. Regarding hardware, we conduct all experiments on two Nvidia GeForce 3090 GPUs.

### C. Comparisons With Other Methods

We choose several representative methods for comparison, including model-driven and data-driven ones. The parameter settings for model-driven methods are listed in Table I. For a fair comparison, we retrain all data-driven methods according to the basic settings specified in their original papers. All the details of training and testing are consistent with our method. For example, training period is uniformly 100 epochs and initial learning rate is always set to 0.001 for all compared methods. Besides, since most of chosen methods are based on pixel-level segmentation, for fairness, we follow the paradigm of combined detector [32].

1) *Quantitative Comparison*: The quantitative results of different detection methods on three datasets are shown in Table II. From this table, we could have three obvious findings.

TABLE II: Quantitative comparison results of different state-of-the-art methods on three datasets. The best and second best results are highlighted in red and blue, respectively.

Scheme	Methods	Publication	DAUB				ITSdT-15K				IRDST				
			mAP <sub>50</sub>	Precision	Recall	F1	mAP <sub>50</sub>	Precision	Recall	F1	mAP <sub>50</sub>	Precision	Recall	F1	
Model-driven	MaxMean [2]	SPIE 1999	10.71	20.38	53.87	29.57	0.87	10.85	8.74	9.68	0.01	0.28	1.48	0.47	
	TopHat [1]	IPT 2006	16.99	21.69	79.83	34.11	11.61	27.21	43.07	33.35	1.81	18.22	10.60	13.40	
	RLCM [4]	IEEE TGRS 2013	0.02	0.27	5.21	0.51	4.62	15.38	30.76	20.50	1.58	16.28	9.70	12.16	
	HBMLCM [5]	IEEE GRSL 2019	3.90	23.96	16.52	19.56	0.72	7.97	9.37	8.61	1.16	29.14	4.66	8.03	
	PSTNN [24]	RS 2019	17.31	25.56	68.86	37.28	7.99	22.98	35.21	27.81	1.45	16.28	9.70	12.16	
	WSLCM [6]	SP 2020	1.37	11.88	11.57	11.73	2.36	16.78	14.53	15.58	1.69	20.87	8.70	12.28	
	Data-driven	ACM [9]	WACV 2021	64.02	70.96	91.30	79.86	55.38	78.37	71.69	74.88	52.40	76.33	69.32	72.66
RISTD [43]		IEEE GRSL 2022	81.05	83.46	98.27	90.26	60.47	85.49	71.60	77.93	66.57	84.70	79.63	82.08	
ISNet [10]		CVPR 2022	83.43	89.36	94.99	92.09	62.29	83.46	75.32	79.18	59.78	80.24	75.08	77.58	
UIUNet [17]		IEEE TIP 2022	86.41	94.46	92.03	93.23	65.15	84.07	78.39	81.13	56.38	80.95	70.29	75.25	
SANet [44]		ICASSP 2023	87.12	93.44	94.93	94.18	62.17	87.78	71.23	78.64	64.54	84.29	77.02	80.49	
AGPCNet [14]		IEEE TAES 2023	76.72	82.29	94.43	87.95	67.27	<b>91.19</b>	74.77	82.16	59.21	79.47	75.51	77.44	
RDIAN [15]		IEEE TGRS 2023	84.92	88.20	97.27	92.51	68.49	90.56	76.06	82.68	59.08	77.99	76.35	77.16	
DNANet [12]		IEEE TIP 2023	89.93	92.49	98.27	95.29	70.46	88.55	80.73	84.46	63.61	82.92	77.48	80.11	
DTUM [31]		IEEE TNNLS 2023	85.86	87.54	<b>99.79</b>	93.26	67.97	77.95	<b>88.28</b>	82.79	71.48	82.87	<b>87.79</b>	<b>85.26</b>	
SIRST5K [45]		IEEE TGRS 2024	93.31	97.78	96.93	97.35	61.52	86.95	71.32	78.36	52.28	76.12	69.07	72.42	
MShNet [46]		CVPR 2024	85.97	93.13	93.12	93.13	60.82	89.69	68.44	77.64	63.21	82.31	77.64	79.91	
RPCANet [19]		WACV 2024	85.98	89.38	97.56	93.29	62.28	81.46	77.10	79.22	56.50	77.77	73.80	75.73	
TMP [56]		ESWA 2024	92.87	98.01	95.04	96.50	<b>77.73</b>	<b>92.97</b>	84.74	<b>88.67</b>	70.03	86.70	81.41	83.97	
ST-Trans [57]		TGRS 2024	92.73	97.75	95.52	96.62	76.02	89.96	85.18	87.50	70.04	<b>88.21</b>	80.01	83.91	
SSTNet [32]		IEEE TGRS 2024	<b>95.59</b>	<b>98.08</b>	98.10	<b>98.09</b>	76.96	91.05	85.29	88.07	<b>71.55</b>	<b>88.56</b>	81.92	85.11	
Tridos (Ours)		-		<b>97.80</b>	<b>99.20</b>	<b>99.67</b>	<b>99.43</b>	<b>80.41</b>	90.71	<b>90.60</b>	<b>90.65</b>	<b>73.72</b>	84.49	<b>89.35</b>	<b>86.85</b>

Firstly, model-driven methods usually perform bad, almost inefficient. For example, as the SOTA one, PSTNN can only achieve a low mAP<sub>50</sub> of 17.31%, a low Precision of 25.56% and a low Recall of 68.86% on DAUB, far lower than any compared data-driven method in TABLE II. One possible reason is that they rely on hand-crafted features and have almost no adaptively-learning ability to target features.

The second is that our Tridos achieves the best performance on most evaluation metrics over three datasets, especially on mAP<sub>50</sub> and F1 score. For example, on DAUB dataset, Tridos could obtain the highest mAP<sub>50</sub> 97.80% and the highest F1 99.43%. In terms of Recall, the 99.67% by Tridos is only slightly lower than the SOTA 99.79% by SSTNet. Furthermore, on ITSdT-15K, our Tridos still obtains the highest mAP<sub>50</sub> 80.41% and F1 90.65%, far superior to previous SOTA mAP<sub>50</sub> 76.96%, and F1 score 88.07% by SSTNet. Additionally, it also outperforms the comparison methods almost on all metrics on IRDST.

The third is that our Tridos has stronger robustness than other ones. Almost all methods could perform better on DAUB than on ITSdT-15K and IRDST. For example, SOTA SSTNet achieves mAP<sub>50</sub> 95.59% and F1 98.09% on DAUB, while on ITSdT-15K its mAP<sub>50</sub> is 76.96% and F1 is 88.07%. Moreover, its mAP<sub>50</sub> is 71.55% and F1 is 85.11% on IRDST. That could be because ITSdT-15K and IRDST contain more complex scenes with the effects of noise and occlusion. Nevertheless, on DAUB our Tridos achieves a mAP<sub>50</sub> improvement of 2.21% and F1 rise of 1.34% on SSTNet. On ITSdT-15K and IRDST, the mAP<sub>50</sub> increments by Tridos on SSTNet are 3.45% and 2.17%, respectively. Meanwhile, on these two datasets, the F1 increments by Tridos on SSTNet are 2.58% and 1.74%, respectively. These comparisons show that our method could be more tolerant to complex scenarios than others.

Besides, the comparisons on IRDST indicate that our method achieves higher F1 score than SOTA SSTNet. However, its precision 84.49% is 4.13% lower than the 88.56% by SSTNet under same IOU threshold 0.65. One main reason is

that our triple-domain feature learning method tends to detect all targets as many as possible, avoiding miss detection. In real application scenes, low miss detection is usually more important than high false detection. Therefore, our method aims to keep high Recall, by balancing Precision. In fact, if threshold is increased, our Precision could be higher than that of SSTNet. For example, experiments show when threshold is set to 0.7, our Precision is 88.71%, 0.15% higher than the 88.56% achieved by SSTNet.

2) *Visual Comparison*: We present the visual comparisons of different detection methods in Fig. 5 - Fig. 7. It is evident that our proposed method could usually accurately detect moving infrared small targets. In contrast, other ones often lead to miss detection or false detection.

For example, in Fig. 5, on DAUB, our Tridos precisely detects the target occluded by trees. However, ACM, RISTD, AGPC and RPCA cause miss detection. Some methods incorrectly treat a bright spot as a target, producing false detection, such as ISNet, DTUM, SIRST5K and ST-Trans. Moreover, in Fig. 6, on ITSdT-15K, some methods fail to detect all targets, such as ACM, DNANet, RPCA and SSTNet. RISTD even detects seven targets, causing false detection. Meanwhile, in Fig. 7, on IRDST, SANet, DNANet and DTUM appear false detection. Furthermore, ST-Trans seems to have a smaller bounding box than ground truth. Some methods cannot even detect any targets, such as AGPC, SIRST5K and RPCA. In contrast, our Tridos could obtain the bounding boxes with the largest similarity to ground truth. In summary, we can observe that the qualitative results of these visualizations are much consistent to the quantitative results in Table II, indicating the superiority of our method.

3) *PR Curve Comparison*: To evaluate the comprehensive performance of different methods, we draw three groups of Precision-Recall (PR) curves on DAUB, ITSdT-15K and IRDST, as shown in Fig. 8. By comparison, we could easily observe that our curves are almost always above other ones on three datasets. The larger a curve envelope area is, the better



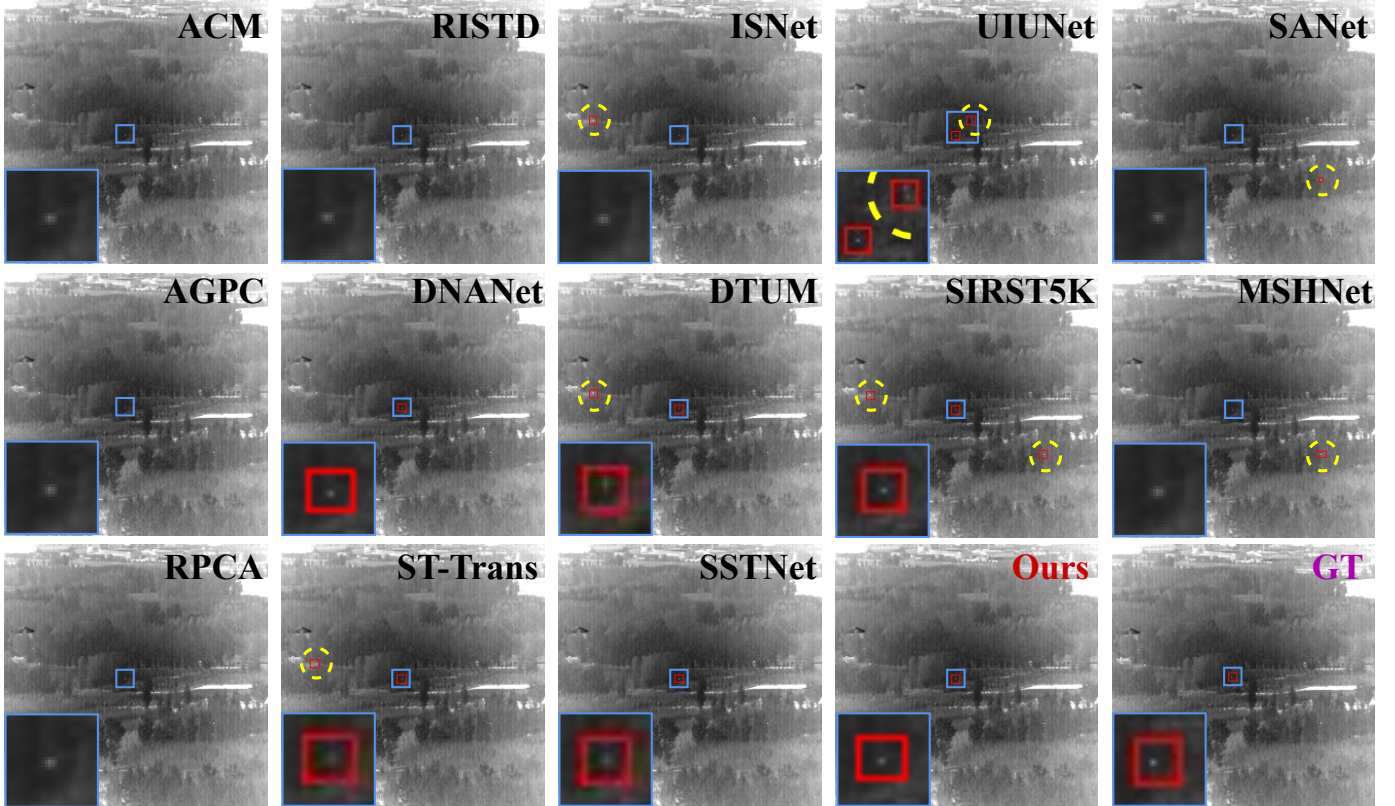


Fig. 5: The visualization comparisons of 14 methods on DAUB, with 21/63.bmp. GT is ground truth. Red and blue boxes represent detected targets and amplified detection regions, respectively. Yellow circles denote false alarms.

a method is. Therefore, the three groups of PR curves indicate that our Tridos has the best comprehensive performance with an optimal balance between Precision and Recall.

TABLE III: The comparative results of model complexity on ITSDD-15K. The best results are marked in bold.

Methods	Frames	mAP <sub>50</sub> ↑	F1 ↑	Params ↓	GFlops ↓	FPS ↑
ACM [9]	1	55.38	74.88	3.04M	<b>24.73</b>	<b>29.11</b>
RISTD [43]	1	60.47	77.93	3.28M	76.28	10.21
ISNet [10]	1	62.29	79.18	3.49M	265.73	11.20
UIUNet [17]	1	65.15	81.13	53.06M	456.70	3.63
SANet [44]	1	62.17	78.64	12.40M	42.04	10.55
AGPCNet [14]	1	67.27	82.16	14.88M	366.15	4.79
RDIAN [15]	1	68.49	82.68	<b>2.74M</b>	50.44	20.52
DNANet [12]	1	70.46	84.46	7.22M	135.24	4.82
SIRST5K [45]	1	61.52	78.36	11.48M	182.61	7.37
MSHNet [46]	1	60.82	77.64	6.59M	69.59	18.55
RPCANet [19]	1	62.28	79.22	3.21M	382.69	15.89
DTUM [31]	5	67.97	82.79	9.64M	128.16	14.28
TMP [56]	5	77.73	88.67	16.41M	92.85	6.91
ST-Trans [57]	5	76.02	87.50	38.13M	145.16	3.90
SSTNet [32]	5	76.96	88.07	11.95M	123.60	7.37
Ours	5	<b>80.41</b>	<b>90.65</b>	14.13M	130.72	13.71

4) *Model Complexity Comparison*: We compare the model complexity of our Tridos with fifteen representative methods in Table III, mainly including *Params*, *GFlops* and *FPS*. In this table, we could obviously have two discoveries.

One is that our Tridos has a slight increase in *Params* and *GFlops*. For example, the smallest *Params* in multi-frame methods is 9.64M by DTUM. the best *GFlops* in multi-frame methods is 92.85 by TMP. Our Tridos has a medium *Params* 14.13M and *GFlops* 130.72. One probable reason is that

DTUM and TMP are based on spatio-temporal domains, while Tridos introduces frequency domain, besides spatio-temporal domains. It could be because that converting spatio-domain data into frequency domain involves some additional computations, such as the Fourier transform. Moreover, our network needs extra convolutional layers to coordinate frequency domain features and integrating different domain features further raises *Params* and *GFlops*. Nevertheless, achieving obvious performance gains, these complexity costs are acceptable and worthwhile.

The other is that computational cost increase results in a middle inference speed of FPS 13.71. Besides, each multi-frame method will process five frame images in inference, so its FPS is often lower than that of a single-frame one, e.g., ACM, RDIAN, MSHNet and RPCANet. Nevertheless, our FPS still seems higher than that by RISTD, ISNet, UIUNet, AGPCNet, DNANet, SIRST5K, ST-Trans and SSTNet.

#### D. Ablation Study

1) *Effects of Different Components*: We conduct four groups of ablation studies on DAUB and ITSDD-15K to investigate the effects of each component on our Tridos, as shown in Tables IV - VIII.

In Table IV, we could have two findings. One is that each component improves detection performance to some extent. For example, on DAUB the baseline without any components only acquires mAP<sub>50</sub> 84.43% and F1 92.50%. Once MSRM is applied, mAP<sub>50</sub> increases from 84.43% to 92.17%, and F1

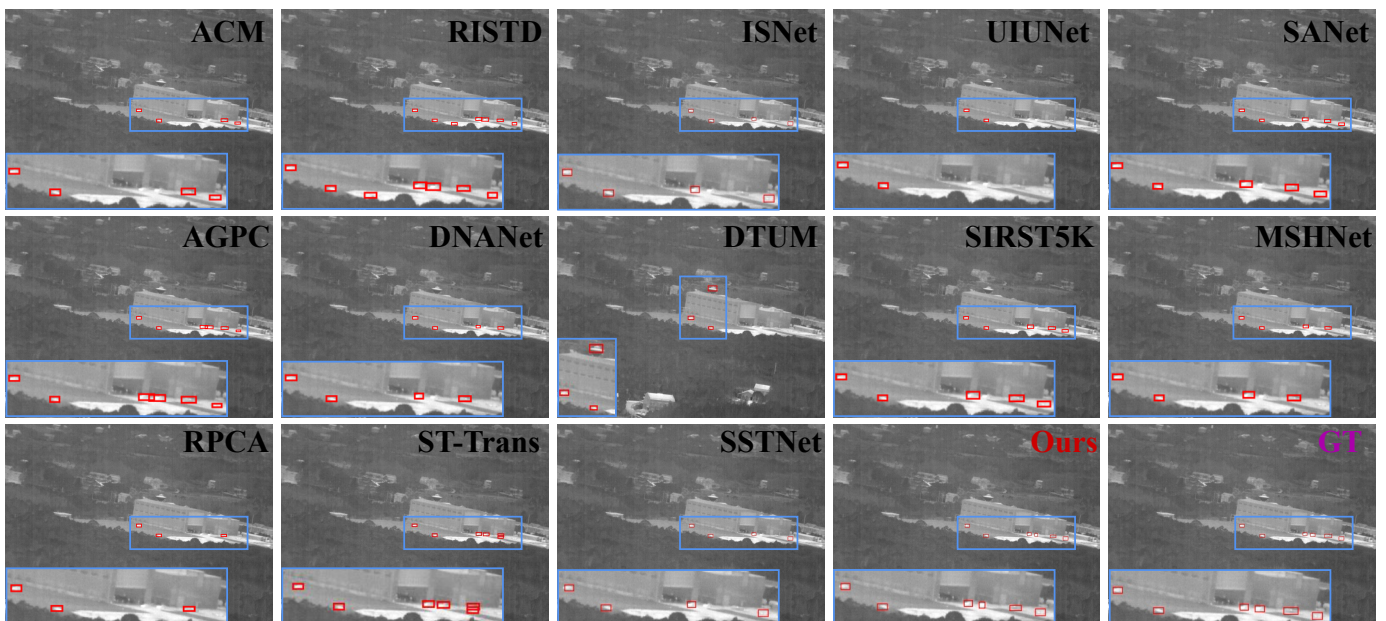


Fig. 6: The visualization comparisons of 14 methods on ITSdT-15K, with 82/205.bmp. GT is ground truth. Red and blue boxes represent detected targets and amplified detection regions, respectively.

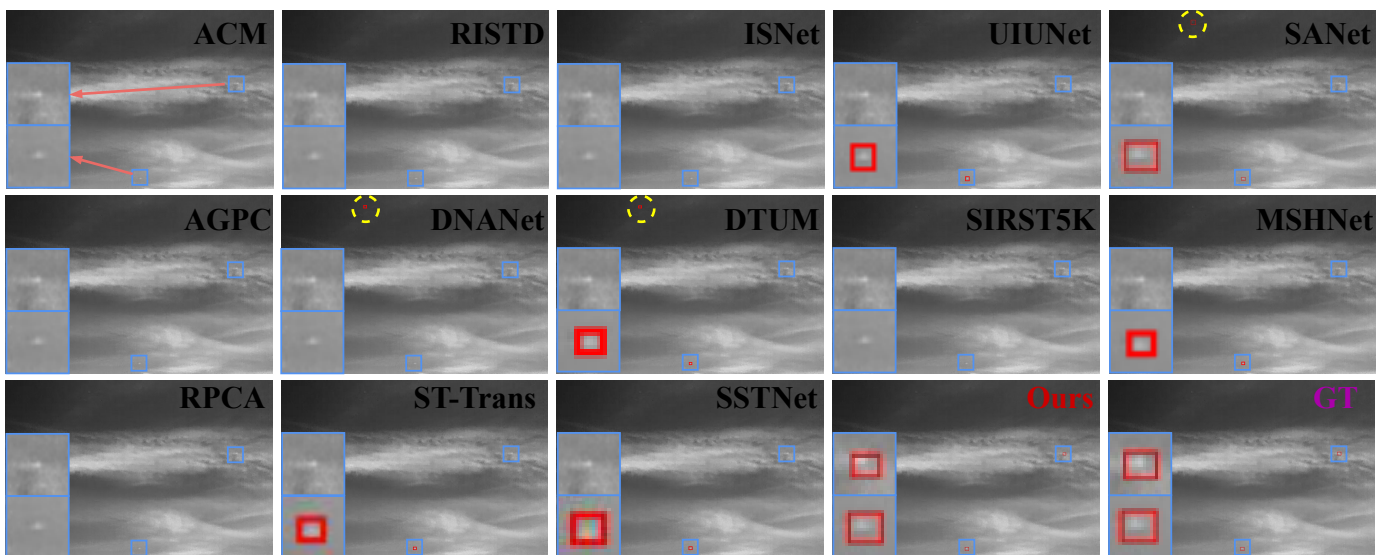


Fig. 7: The visualization comparisons of 14 methods on IRDST, with 6/51.bmp. GT is ground truth. Red and blue boxes represent detected targets and amplified detection regions, respectively. Yellow circles denote false alarms.

rises from 92.50% to 94.39%. with TDEM,  $mAP_{50}$  and F1 could be further improved to 93.73% and 95.37%, respectively. Furthermore, adding frequency domain (w/o RCU) could also provide an obvious gain, with  $mAP_{50}$  and F1 respectively rising to 95.61% and 97.09%. Besides, Tridos performs variably with different kinds of RCUs (A, B and C). The other is that the best performance could be obtained by applying all components together. For example, with all components, on DAUB  $mAP_{50}$  and F1 are increased to 97.80% and 99.43%, respectively. On ITSdT-15K,  $mAP_{50}$  and F1 are also refreshed to 80.41% and 90.65%, respectively.

2) *Effects of NAB and MEU in MSRM*: To explore the potential contribution of NAB and MEU to MSRM more

deeply, we conduct a group of ablation studies, as shown in Table V. In it, MEU plays an essential role on modeling inter-frame spatial relationships. For example, with MEU, on DAUB  $mAP_{50}$  and F1 could be increased from 94.92% to 97.80%, and 98.19% to 99.43%, respectively. It implies the effectiveness of adopted memory mechanism. Similarly, on ITSdT-15K, NAB could improve  $mAP_{50}$  from 78.49% to 80.41%, and F1 is raised from 89.08% to 90.65%. These effects could be attributed to the ability of NAB to capture long-distance dependencies.

To verify the motivation of devising NAB and distinguish it from self-attention mechanism, we perform a group of ablation experiments, as shown in Table VI. ‘Conv’ represents

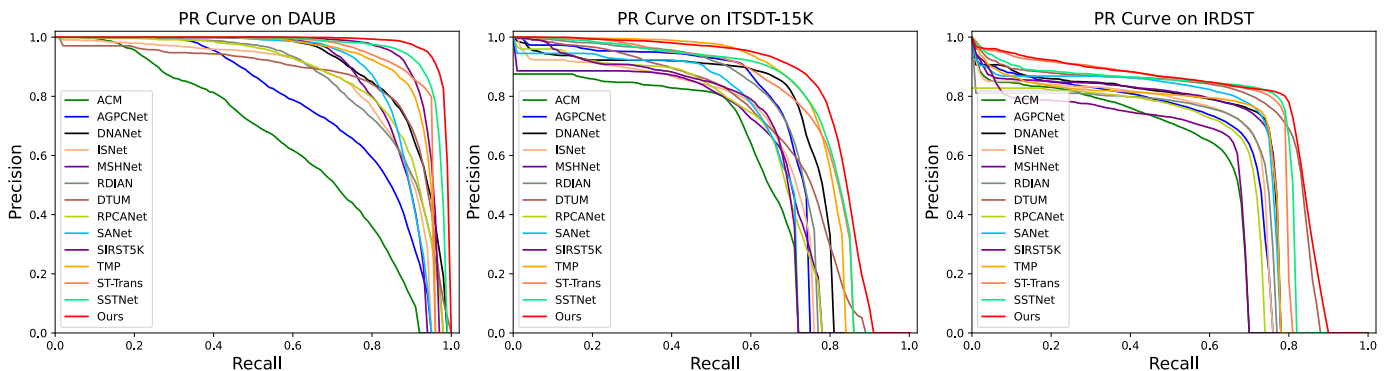


Fig. 8: PR curves of 14 representative detection methods on datasets DAUB, ITSdT-15K and IRDST.

TABLE IV: Ablation study on 4 different components, including MSRM, TDEM, LGFM and RCU, on two datasets. RCU(A) only uses RCU<sub>1</sub>, while RCU(B) uses both RCU<sub>1</sub> and RCU<sub>2</sub>. RCU(C) uses all RCU components.

Settings	MSRM	TDEM	LGFM	RCU (A)	RCU (B)	RCU (C)	DAUB				ITSdT-15K			
							mAP <sub>50</sub>	Precision	Recall	F1	mAP <sub>50</sub>	Precision	Recall	F1
w/o All	-	-	-	-	-	-	84.43	89.73	95.45	92.50	71.95	83.43	87.35	85.34
w MSRM	✓	-	-	-	-	-	92.17	94.92	93.86	94.39	75.36	83.57	91.19	87.21
w MSRM & TDEM	✓	✓	-	-	-	-	93.73	94.51	96.24	95.37	76.77	87.03	89.72	88.35
w/o RCU	✓	✓	✓	-	-	-	95.61	96.81	97.37	97.09	78.24	85.83	<b>92.06</b>	88.84
w RCU(A)	✓	✓	✓	✓	-	-	95.74	97.61	97.12	97.36	79.08	89.66	89.50	89.58
w RCU(B)	✓	✓	✓	-	✓	-	96.25	98.00	99.33	98.66	79.68	89.36	90.10	89.73
w RCU(C)	✓	✓	✓	-	-	✓	<b>97.80</b>	<b>99.20</b>	<b>99.67</b>	<b>99.43</b>	<b>80.41</b>	<b>90.71</b>	90.60	<b>90.65</b>

TABLE V: Ablation study on NAB and MEU of MSRM.

Settings	DAUB				ITSdT-15K			
	mAP <sub>50</sub>	Precision	Recall	F1	mAP <sub>50</sub>	Precision	Recall	F1
MSRM w/o NAB	96.53	98.24	99.52	98.88	78.49	88.03	90.16	89.08
MSRM w/o MEU	94.92	97.57	98.81	98.19	74.05	84.91	88.74	86.78
MSRM w/o All	93.47	95.33	99.04	97.15	73.16	85.67	86.29	85.97
MSRM	<b>97.80</b>	<b>99.20</b>	<b>99.67</b>	<b>99.43</b>	<b>80.41</b>	<b>90.71</b>	<b>90.60</b>	<b>90.65</b>

a baseline adopting convolutional layers rather than attention blocks. We observe that attention mechanism could improve baseline performance. Specifically, on DAUB, self-attention could improve mAP<sub>50</sub> from 94.98% to 96.64% and F1 from 97.12% to 98.59%. NAB could further raise mAP<sub>50</sub> to 97.80% and F1 to 99.43%. In detail, self-attention catches the dependencies in sequences by computing the attention scores of all position pairs. In contrast, NAB focuses more on capturing comprehensive contexts and long-distance dependencies.

TABLE VI: Ablation study on the effectiveness of NAB and self-attention module.

Settings	DAUB				ITSdT-15K			
	mAP <sub>50</sub>	Precision	Recall	F1	mAP <sub>50</sub>	Precision	Recall	F1
Conv	94.98	96.76	97.48	97.12	77.18	86.43	88.71	87.56
Self-attention	96.64	98.07	99.12	98.59	78.53	87.64	89.23	88.43
NAB	<b>97.80</b>	<b>99.20</b>	<b>99.67</b>	<b>99.43</b>	<b>80.41</b>	<b>90.71</b>	<b>90.60</b>	<b>90.65</b>

3) *Effects of ResB in TDEM*: From Table VII, it is obvious that two residual blocks will make Triods to get the best performance. For example, on ITSdT-15K, the TDEM without residual blocks (TDEM w/o All) only obtains mAP<sub>50</sub> 74.05% and F1 86.78%. With ResB1 (TDEM w ResB1), mAP<sub>50</sub> and F1 will raise to 76.25% and 87.69%, respectively. Moreover, with both (TDEM), mAP<sub>50</sub> and F1 further increase 4.13% and 2.27%, respectively. These improvements could be because both enhance differential information from multiple perspectives, capturing more representative motion features.

TABLE VII: Ablation study on two residual blocks of TDEM.

Settings	DAUB				ITSdT-15K			
	mAP <sub>50</sub>	Precision	Recall	F1	mAP <sub>50</sub>	Precision	Recall	F1
TDEM w/o ResB1	95.49	98.08	98.87	98.48	77.21	86.58	90.25	88.38
TDEM w/o ResB2	94.45	96.24	99.42	97.80	76.25	84.57	91.05	87.69
TDEM w/o All	93.89	96.37	98.87	97.60	74.05	84.91	88.74	86.78
TDEM	<b>97.80</b>	<b>99.20</b>	<b>99.67</b>	<b>99.43</b>	<b>80.41</b>	<b>90.71</b>	<b>90.60</b>	<b>90.65</b>

4) *Effects of FT, ConvB, and SwinB in LGFM*: Additionally, we investigate the effects of *Fourier Transform* (FT), *Conv Branch* (ConvB) and *Swin Transformer Branch* (SwinB) in Table VIII. From it, we could have two apparent findings. First, the global contexts acquired by SwinB is as valuable as the local features obtained by ConvB. For example, on DAUB, without ConvB (LGFM w/o ConvB), it obtains an mAP<sub>50</sub> 95.95% and an F1 98.72%. Without SwinB, it achieves an mAP<sub>50</sub> 95.76% and an F1 98.39%. Second, frequency transformation is a crucial strategy for detecting small targets. For example, on ITSdT-15K, “LGFM w/o FT” only acquires an mAP<sub>50</sub> 73.54% and an F1 85.47%, even assembled with both branches. It could prove that our LGFM is a successful strategy for perceiving frequency information.

TABLE VIII: Ablation study of Fourier transform (FT), the ConvB and SwinB of LGFM.

Settings	DAUB				ITSdT-15K			
	mAP <sub>50</sub>	Precision	Recall	F1	mAP <sub>50</sub>	Precision	Recall	F1
LGFM w/o ConvB	95.95	98.61	98.94	98.72	76.73	86.04	90.35	88.14
LGFM w/o SwinB	95.76	97.52	99.27	98.39	74.77	82.01	92.37	86.88
LGFM w/o FT	94.27	97.46	97.60	97.53	73.54	86.38	84.59	85.47
LGFM w/o All	92.93	97.14	96.45	96.80	72.90	80.64	89.61	84.89
LGFM w All	<b>97.80</b>	<b>99.20</b>	<b>99.67</b>	<b>99.43</b>	<b>80.41</b>	<b>90.71</b>	<b>90.60</b>	<b>90.65</b>

To demonstrate the effectiveness of frequency learning, we select four samples from DAUB and ITSdT-15K, and visualize the features before and after LGFM, as shown in Fig. 9. In it, we could have two findings. One is that the feature map

by “w LGFM” eliminates some background noise interference. This demonstrates that LGFM could effectively filter irrelevant information. The other is that after applying LGFM, the feature response to targets is obviously stronger. This comparison implies that LGFM could make our network more focused on target regions.

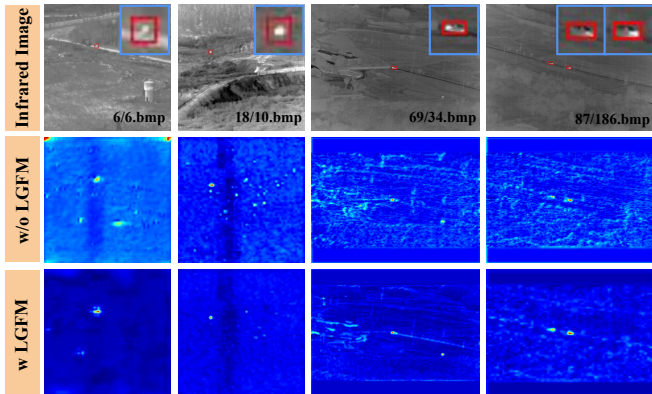


Fig. 9: Feature visualization comparisons before (w/o) and after (w) LGFM. The first two columns are on DAUB, and the rest are on ITSDT-5K.

5) *Effects of CAB and SAB in RCU*: We conduct a group of experiments to validate the effectiveness of CAB and SAB. In Table IX, we could find that integrating CAB and SAB can promote RCU performance, acquiring the best results. For example, on ITSDT-15K, SAB could increase mAP<sub>50</sub> from 76.73% to 77.75%, and F1 from 88.25% to 88.88%. CAB could boost mAP<sub>50</sub> to 78.61% and F1 to 89.03%. Detection performance will peak, i.e., mAP<sub>50</sub> 80.41% and F1 90.65%, only when both CAB and SAB are employed. This is because when CAB and SAB are combined, they could complement each other by capturing spatial and channel dependencies to achieve more robust feature representations.

TABLE IX: Ablation study on the CAB and SAB of RCU.

Settings	DAUB				ITSDT-15K			
	mAP <sub>50</sub>	Precision	Recall	F1	mAP <sub>50</sub>	Precision	Recall	F1
RCU w/o all	92.41	94.24	99.12	96.62	76.73	87.00	89.54	88.25
RCU w SAB	94.20	96.67	99.37	97.69	77.55	86.94	90.90	88.88
RCU w CAB	95.64	97.35	99.58	98.45	78.61	88.23	89.85	89.03
RCU w All	<b>97.80</b>	<b>99.20</b>	<b>99.67</b>	<b>99.43</b>	<b>80.41</b>	<b>90.71</b>	<b>90.60</b>	<b>90.65</b>

6) *Effects of Time Window Size  $T$* : We conduct a group of experiments with different time window sizes to investigate the impact of time window  $T$  on detection performance, as shown in Fig. 10.

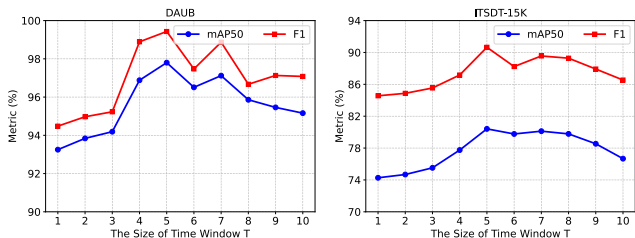


Fig. 10: The effects of time window size  $T$  on Tridos.

Time window size  $T$  could provide contexts for a keyframe. In Fig. 10, we could observe two findings. First, our method obtains the peak detection performance on two datasets when  $T = 5$ . Second, proper  $T$  is crucial for infrared small target detection. For example, when  $T \leq 3$ , increasing  $T$  will result in less gain. when  $T > 3$ , detection performance increment is more evident. Furthermore, when  $T > 5$  a further increase of  $T$  will lead to fluctuation, even a decrease on metrics. This could be explained by the fact that capturing the temporal contexts of consecutive frames would be insufficient if  $T$  is too small. Conversely, if it is too big, there would be a risk of excessive redundant features, causing interference. Considering this, we always set  $T = 5$  in experiments.

7) *Effects of Different Regression Losses*: To validate the impacts of  $\mathcal{L}_{dvr}$ , we further design a group of comparison experiments with three different regression loss functions, as shown in Table X. In this table, “ $\mathcal{L}_{iou}$ ” indicates that the loss term  $\mathcal{L}_{reg}$  in Eq. (19) is set to  $\mathcal{L}_{iou}$ . “ $\mathcal{L}_{nwd}$ ” denotes that  $\mathcal{L}_{reg}$  is set to  $\mathcal{L}_{nwd}$ . Moreover, “ $\mathcal{L}_{dvr}$ ” represents that  $\mathcal{L}_{reg}$  is set to  $\mathcal{L}_{dvr}$ , computed by Eq. (20).

By comparison, our dual-view regression loss, i.e.,  $\mathcal{L}_{dvr}$ , could gain a peak performance on each dataset. For example, on DAUB,  $\mathcal{L}_{iou}$  only realizes 96.15% and 98.56% on mAP<sub>50</sub> and F1, respectively. In contrast,  $\mathcal{L}_{dvr}$  could get 97.80% and 99.43% on mAP<sub>50</sub> and F1, respectively. One possible explanation is that our  $\mathcal{L}_{dvr}$  could improve detection accuracy by minimizing the distribution differences of bounding boxes. In summary, our dual-view regression loss computed on  $\mathcal{L}_{iou}$  and  $\mathcal{L}_{nwd}$  incorporates the advantages of balancing small target localization and bounding box distribution.

TABLE X: Comparisons of three regression loss functions.

Settings	DAUB				ITSDT-15K			
	mAP <sub>50</sub>	Precision	Recall	F1	mAP <sub>50</sub>	Precision	Recall	F1
$\mathcal{L}_{iou}$	96.15	98.09	99.04	98.56	78.20	86.71	89.85	88.25
$\mathcal{L}_{nwd}$	93.66	96.45	98.54	97.48	73.87	82.17	84.45	83.29
$\mathcal{L}_{dvr}$	<b>97.80</b>	<b>99.20</b>	<b>99.67</b>	<b>99.43</b>	<b>80.41</b>	<b>90.71</b>	<b>90.60</b>	<b>90.65</b>

8) *Effects of Different Hyper-parameters*: As shown in Fig. 11, we design two groups of experiments to evaluate the effects of hyper-parameters  $w$  (Swin Transformer window size) and  $c$  (hidden channel number) on Tridos. It is seen that F1 could reach to a peak on DAUB and ITSDT-15K when  $w = 8$ . Similar to this, the highest value of F1 could be obtained when  $c = 128$ . Besides, we could find that Tridos’s detection performance is more sensitive to  $w$  than to  $c$ . Overall, the optimal  $w$  and  $c$  are often 8 and 128, respectively.

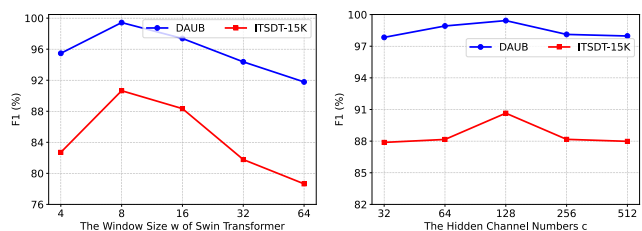


Fig. 11: The effects of hyper-parameters  $w$  and  $c$  on Tridos.

Furthermore, we conduct a group of experiments to analyze the effects of two additional hyper-parameters  $\alpha$  and  $\beta$  in

Eq. (20). As shown in Table XI, we change  $\alpha$  and  $\beta$  to different settings, while keep other parameters fixed. In this table, it is evident that  $\alpha$  and  $\beta$  obviously impact the detection performance of our Tridos. When  $\alpha = 0.5$  and  $\beta = 0.5$ , detection performance will peak. According to Eq. (20), it implies that  $\mathcal{L}_{iou}$  and  $\mathcal{L}_{nwd}$  have the same importance in promoting the detection performance of our Tridos.

TABLE XI: The effects of hyper-parameters  $\alpha$  and  $\beta$ .

Settings ( $\alpha, \beta$ )	DAUB				ITSdT-15K			
	mAP <sub>50</sub>	Precision	Recall	F1	mAP <sub>50</sub>	Precision	Recall	F1
(0.1, 0.9)	94.88	96.74	99.03	97.88	76.94	84.40	92.20	88.13
(0.3, 0.7)	96.27	98.17	99.06	98.61	79.87	90.54	89.50	90.02
(0.5, 0.5)	<b>97.80</b>	<b>99.20</b>	<b>99.67</b>	<b>99.43</b>	<b>80.41</b>	<b>90.71</b>	<b>90.60</b>	<b>90.65</b>
(0.7, 0.3)	95.61	97.42	99.23	98.32	77.63	88.64	89.15	88.89
(0.9, 0.1)	95.16	96.99	99.42	98.19	77.41	86.78	90.84	88.76

9) *Comparison with Swin Transformer and YOLOX*: To further illustrate the effectiveness of our method, we choose conventional Swin-Transformer (SwinT) and YOLOX for performance comparisons, as shown in Table XII.

It could be found that our Tridos with frequency-aware and memory enhancement achieves evidently higher detection metrics on each dataset. For example, on ITSdT-15K, Tridos could acquire an mAP<sub>50</sub> 80.41%, Precision 90.71%, Recall 90.60%, and F1 90.65%, far superior to SwinT and YOLOX. This group of experiments proves that our superiority mainly attributed to proposed triple-domain feature learning, not only to the simple combination of SwinT and YOLOX.

TABLE XII: Comparisons with SwinT and YOLOX.

Methods	DAUB				ITSdT-15K			
	mAP <sub>50</sub>	Precision	Recall	F1	mAP <sub>50</sub>	Precision	Recall	F1
SwinT	83.40	90.46	93.45	91.93	49.93	78.56	64.30	70.72
YOLOX	85.62	90.73	94.75	92.70	72.15	84.43	86.85	85.62
<b>Ours</b>	<b>97.80</b>	<b>99.20</b>	<b>99.67</b>	<b>99.43</b>	<b>80.41</b>	<b>90.71</b>	<b>90.60</b>	<b>90.65</b>

## V. CONCLUSIONS

For extending feature learning, this paper proposes Tridos to capture the spatio-temporal-frequency features of moving infrared small targets. It enhances spatio-temporal feature representation through frequency domain and models inter-frame spatial relationships by memory enhancement mechanism. To comprehensively evaluate detection methods, an additional dataset ITSdT-15K is collected. The comparison experiments on DAUB, IRDST and ITSdT-15K prove the superiority of our Tridos to existing SOTA methods. Moreover, ablation studies further verify the effectiveness and merits of all elaborately-designed components, including MSRM, TDEM, LGFM and RCU in our Tridos. One obvious weakness of our method is that it could also be with high model complexity and computation cost, just as most data-driven ones. In future work, how to efficiently learn infrared small target features by lightweight neural networks in spatio-temporal-frequency domains is worthy of further exploring.

## REFERENCES

- [1] X. Bai and F. Zhou, "Analysis of new top-hat transformation and the application for infrared dim small target detection," *Pattern Recognition*, vol. 43, no. 6, pp. 2145–2156, 2010.
- [2] S. D. Deshpande, M. H. Er, R. Venkateswarlu, and P. Chan, "Max-mean and max-median filters for detection of small targets," in *Signal and Data Processing of Small Targets 1999*, vol. 3809. SPIE, 1999, pp. 74–83.
- [3] C. P. Chen, H. Li, Y. Wei, T. Xia, and Y. Y. Tang, "A local contrast method for small infrared target detection," *IEEE Transactions on Geoscience and Remote Sensing*, vol. 52, no. 1, pp. 574–581, 2013.
- [4] J. Han, K. Liang, B. Zhou, X. Zhu, J. Zhao, and L. Zhao, "Infrared small target detection utilizing the multiscale relative local contrast measure," *IEEE Geoscience and Remote Sensing Letters*, vol. 15, no. 4, pp. 612–616, 2018.
- [5] J. Han, S. Moradi, I. Faramarzi, C. Liu, H. Zhang, and Q. Zhao, "A local contrast method for infrared small-target detection utilizing a tri-layer window," *IEEE Geoscience and Remote Sensing Letters*, vol. 17, no. 10, pp. 1822–1826, 2019.
- [6] J. Han, S. Moradi, I. Faramarzi, H. Zhang, Q. Zhao, X. Zhang, and N. Li, "Infrared small target detection based on the weighted strengthened local contrast measure," *IEEE Geoscience and Remote Sensing Letters*, vol. 18, no. 9, pp. 1670–1674, 2020.
- [7] C. Gao, D. Meng, Y. Yang, Y. Wang, X. Zhou, and A. G. Hauptmann, "Infrared patch-image model for small target detection in a single image," *IEEE Transactions on Image Processing*, vol. 22, no. 12, pp. 4996–5009, 2013.
- [8] X. Wang, Z. Peng, D. Kong, and Y. He, "Infrared dim and small target detection based on stable multisubspace learning in heterogeneous scene," *IEEE Transactions on Geoscience and Remote Sensing*, vol. 55, no. 10, pp. 5481–5493, 2017.
- [9] Y. Dai, Y. Wu, F. Zhou, and K. Barnard, "Asymmetric Contextual Modulation for Infrared Small Target Detection," in *2021 IEEE Winter Conference on Applications of Computer Vision (WACV)*, 2021, pp. 949–958.
- [10] M. Zhang, R. Zhang, Y. Yang, H. Bai, J. Zhang, and J. Guo, "ISNet: Shape matters for infrared small target detection," in *Proceedings of the IEEE/CVF Conference on Computer Vision and Pattern Recognition*, 2022, pp. 877–886.
- [11] H. Wang, L. Zhou, and L. Wang, "Miss detection vs. false alarm: Adversarial learning for small object segmentation in infrared images," in *Proceedings of the IEEE/CVF International Conference on Computer Vision*, 2019, pp. 8509–8518.
- [12] B. Li, C. Xiao, L. Wang, Y. Wang, Z. Lin, M. Li, W. An, and Y. Guo, "Dense nested attention network for infrared small target detection," *IEEE Transactions on Image Processing*, vol. 32, pp. 1745–1758, 2022.
- [13] Y. Dai, Y. Wu, F. Zhou, and K. Barnard, "Attentional local contrast networks for infrared small target detection," *IEEE Transactions on Geoscience and Remote Sensing*, vol. 59, no. 11, pp. 9813–9824, 2021.
- [14] T. Zhang, L. Li, S. Cao, T. Pu, and Z. Peng, "Attention-Guided Pyramid Context Networks for Detecting Infrared Small Target Under Complex Background," *IEEE Transactions on Aerospace and Electronic Systems*, vol. 59, no. 4, pp. 4250–4261, 2023.
- [15] H. Sun, J. Bai, F. Yang, and X. Bai, "Receptive-Field and Direction Induced Attention Network for Infrared Dim Small Target Detection With a Large-Scale Dataset IRDST," *IEEE Transactions on Geoscience and Remote Sensing*, vol. 61, pp. 1–13, 2023.
- [16] J. Lin, S. Li, L. Zhang, X. Yang, B. Yan, and Z. Meng, "IR-TransDet: Infrared Dim and Small Target Detection With IR-Transformer," *IEEE Transactions on Geoscience and Remote Sensing*, vol. 61, pp. 1–13, 2023.
- [17] X. Wu, D. Hong, and J. Chanussot, "UIU-Net: U-Net in U-Net for infrared small object detection," *IEEE Transactions on Image Processing*, vol. 32, pp. 364–376, 2022.
- [18] B. Yang, X. Zhang, J. Zhang, J. Luo, M. Zhou, and Y. Pi, "EFLNet: Enhancing Feature Learning Network for Infrared Small Target Detection," *IEEE Transactions on Geoscience and Remote Sensing*, vol. 62, pp. 1–11, 2024.
- [19] F. Wu, T. Zhang, L. Li, Y. Huang, and Z. Peng, "RPCANet: Deep Unfolding RPCA Based Infrared Small Target Detection," in *Proceedings of the IEEE/CVF Winter Conference on Applications of Computer Vision*, 2024, pp. 4809–4818.
- [20] C. Kwan and B. Budavari, "Enhancing small moving target detection performance in low-quality and long-range infrared videos using optical flow techniques," *Remote Sensing*, vol. 12, no. 24, p. 4024, 2020.
- [21] F. Zhao, T. Wang, S. Shao, E. Zhang, and G. Lin, "Infrared Moving Small-Target Detection via Spatiotemporal Consistency of Trajectory Points," *IEEE Geoscience and Remote Sensing Letters*, vol. 17, no. 1, pp. 122–126, 2020.

- [22] F. Wu, H. Yu, A. Liu, J. Luo, and Z. Peng, "Infrared Small Target Detection Using Spatiotemporal 4-D Tensor Train and Ring Unfolding," *IEEE Transactions on Geoscience and Remote Sensing*, 2023.
- [23] Y. Luo, X. Li, and S. Chen, "Feedback Spatial-Temporal Infrared Small Target Detection based on Orthogonal Subspace Projection," *IEEE Transactions on Geoscience and Remote Sensing*, 2024.
- [24] G. Wang, B. Tao, X. Kong, and Z. Peng, "Infrared small target detection using nonoverlapping patch spatial-temporal tensor factorization with capped nuclear norm regularization," *IEEE Transactions on Geoscience and Remote Sensing*, vol. 60, pp. 1–17, 2021.
- [25] T. Liu, J. Yang, B. Li, C. Xiao, Y. Sun, Y. Wang, and W. An, "Nonconvex tensor low-rank approximation for infrared small target detection," *IEEE Transactions on Geoscience and Remote Sensing*, vol. 60, pp. 1–18, 2021.
- [26] F. Zhang, C. Li, and L. Shi, "Detecting and tracking dim moving point target in IR image sequence," *Infrared Physics & Technology*, vol. 46, no. 4, pp. 323–328, 2005.
- [27] X. Ren, J. Wang, T. Ma, K. Bai, M. Ge, and Y. Wang, "Infrared dim and small target detection based on three-dimensional collaborative filtering and spatial inversion modeling," *Infrared physics & technology*, vol. 101, pp. 13–24, 2019.
- [28] X. Sun, X. Liu, Z. Tang, G. Long, and Q. Yu, "Real-time visual enhancement for infrared small dim targets in video," *Infrared physics & technology*, vol. 83, pp. 217–226, 2017.
- [29] J. Du, H. Lu, L. Zhang, M. Hu, S. Chen, Y. Deng, X. Shen, and Y. Zhang, "A spatial-temporal feature-based detection framework for infrared dim small target," *IEEE Transactions on Geoscience and Remote Sensing*, vol. 60, pp. 1–12, 2021.
- [30] P. Yan, R. Hou, X. Duan, C. Yue, X. Wang, and X. Cao, "STDMA-Net: Spatio-temporal differential multiscale attention network for small moving infrared target detection," *IEEE Transactions on Geoscience and Remote Sensing*, vol. 61, pp. 1–16, 2023.
- [31] R. Li, W. An, C. Xiao, B. Li, Y. Wang, M. Li, and Y. Guo, "Direction-coded temporal U-shape module for multiframe infrared small target detection," *IEEE Transactions on Neural Networks and Learning Systems*, 2023.
- [32] S. Chen, L. Ji, J. Zhu, M. Ye, and X. Yao, "SSTNet: Sliced Spatio-Temporal Network With Cross-Slice ConvLSTM for Moving Infrared Dim-Small Target Detection," *IEEE Transactions on Geoscience and Remote Sensing*, vol. 62, pp. 1–12, 2024.
- [33] X. Tong, Z. Zuo, S. Su, J. Wei, X. Sun, P. Wu, and Z. Zhao, "ST-Trans: Spatial-Temporal Transformer for Infrared Small Target Detection in Sequential Images," *IEEE Transactions on Geoscience and Remote Sensing*, 2024.
- [34] R. Fu, H. Fan, Y. Zhu, B. Hui, Z. Zhang, P. Zhong, D. Li, S. Zhang, G. Chen, and L. Wang, "A dataset for infrared time-sensitive target detection and tracking for air-ground application," May 2022.
- [35] Z. Ge, S. Liu, F. Wang, Z. Li, and J. Sun, "YOLOX: Exceeding yolo series in 2021," *arXiv preprint arXiv:2107.08430*, 2021.
- [36] T.-Y. Lin, M. Maire, S. Belongie, J. Hays, P. Perona, D. Ramanan, P. Dollár, and C. L. Zitnick, "Microsoft coco: Common objects in context," in *Computer Vision—ECCV 2014: 13th European Conference, Zurich, Switzerland, September 6–12, 2014, Proceedings, Part V 13*. Springer, 2014, pp. 740–755.
- [37] J. W. Cooley, P. A. Lewis, and P. D. Welch, "The fast Fourier transform and its applications," *IEEE Transactions on Education*, vol. 12, no. 1, pp. 27–34, 1969.
- [38] Z. Liu, J. Ning, Y. Cao, Y. Wei, Z. Zhang, S. Lin, and H. Hu, "Video Swin Transformer," in *Proceedings of the IEEE/CVF conference on computer vision and pattern recognition*, 2022, pp. 3202–3211.
- [39] T.-Y. Lin, P. Goyal, R. Girshick, K. He, and P. Dollár, "Focal loss for dense object detection," in *Proceedings of the IEEE International Conference on Computer Vision*, 2017, pp. 2980–2988.
- [40] C. Xu, J. Wang, W. Yang, H. Yu, L. Yu, and G.-S. Xia, "Detecting tiny objects in aerial images: A normalized wasserstein distance and a new benchmark," *ISPRS Journal of Photogrammetry and Remote Sensing*, vol. 190, pp. 79–93, 2022.
- [41] Z. Zheng, P. Wang, D. Ren, W. Liu, R. Ye, Q. Hu, and W. Zuo, "Enhancing geometric factors in model learning and inference for object detection and instance segmentation," *IEEE Transactions on Cybernetics*, vol. 52, no. 8, pp. 8574–8586, 2021.
- [42] B. Hui, Z. Song, H. Fan, P. Zhong, W. Hu, X. Zhang, J. Lin, H. Su, W. Jin, Y. Zhang, and Y. Bai, "A dataset for infrared image dim-small aircraft target detection and tracking under ground / air background," Oct. 2019.
- [43] Q. Hou, Z. Wang, F. Tan, Y. Zhao, H. Zheng, and W. Zhang, "RISTDnet: Robust infrared small target detection network," *IEEE Geoscience and Remote Sensing Letters*, vol. 19, pp. 1–5, 2021.
- [44] J. Zhu, S. Chen, L. Li, and L. Ji, "SANet: Spatial attention network with global average contrast learning for infrared small target detection," in *ICASSP 2023-2023 IEEE International Conference on Acoustics, Speech and Signal Processing (ICASSP)*. IEEE, 2023, pp. 1–5.
- [45] Y. Lu, Y. Lin, H. Wu, X. Xian, Y. Shi, and L. Lin, "SIRST-5K: Exploring Massive Negatives Synthesis with Self-supervised Learning for Robust Infrared Small Target Detection," *IEEE Transactions on Geoscience and Remote Sensing*, 2024.
- [46] Q. Liu, R. Liu, B. Zheng, H. Wang, and Y. Fu, "Infrared small target detection with scale and location sensitivity," in *Proceedings of the IEEE/CVF Computer Vision and Pattern Recognition*, 2024.
- [47] R. Kou, C. Wang, Z. Peng, Z. Zhao, Y. Chen, J. Han, F. Huang, Y. Yu, and Q. Fu, "Infrared small target segmentation networks: A survey," *Pattern Recognition*, vol. 143, p. 109788, 2023.
- [48] M. Zhao, W. Li, L. Li, J. Hu, P. Ma, and R. Tao, "Single-frame infrared small-target detection: A survey," *IEEE Geoscience and Remote Sensing Magazine*, vol. 10, no. 2, pp. 87–119, 2022.
- [49] X. Bai and Y. Bi, "Derivative entropy-based contrast measure for infrared small-target detection," *IEEE Transactions on Geoscience and Remote Sensing*, vol. 56, no. 4, pp. 2452–2466, 2018.
- [50] K. Xu, M. Qin, F. Sun, Y. Wang, Y.-K. Chen, and F. Ren, "Learning in the frequency domain," in *Proceedings of the IEEE/CVF conference on computer vision and pattern recognition*, 2020, pp. 1740–1749.
- [51] J. Li, L.-Y. Duan, X. Chen, T. Huang, and Y. Tian, "Finding the secret of image saliency in the frequency domain," *IEEE Transactions on Pattern Analysis and Machine Intelligence*, vol. 37, no. 12, pp. 2428–2440, 2015.
- [52] S. Chen, L. Ji, S. Zhu, and M. Ye, "MICPL: Motion-Inspired Cross-Pattern Learning for Small-Object Detection in Satellite Videos," *IEEE Transactions on Neural Networks and Learning Systems*, pp. 1–14, 2024.
- [53] S. Chen, J. Zhu, L. Ji, H. Pan, and Y. Xu, "Augtarget data augmentation for infrared small target detection," in *ICASSP 2023-2023 IEEE International Conference on Acoustics, Speech and Signal Processing (ICASSP)*. IEEE, 2023, pp. 1–5.
- [54] L. Wang, Z. Tong, B. Ji, and G. Wu, "TDN: Temporal difference networks for efficient action recognition," in *Proceedings of the IEEE/CVF conference on computer vision and pattern recognition*, 2021, pp. 1895–1904.
- [55] Y. Xiao, Q. Yuan, K. Jiang, X. Jin, J. He, L. Zhang, and C.-w. Lin, "Local-global temporal difference learning for satellite video super-resolution," *IEEE Transactions on Circuits and Systems for Video Technology*, 2023.
- [56] S. Zhu, L. Ji, J. Zhu, S. Chen, and W. Duan, "TMP: Temporal Motion Perception with spatial auxiliary enhancement for moving Infrared dim-small target detection," *Expert Systems with Applications*, p. 124731, 2024.
- [57] X. Tong, Z. Zuo, S. Su, J. Wei, X. Sun, P. Wu, and Z. Zhao, "ST-Trans: Spatial-Temporal Transformer for Infrared Small Target Detection in Sequential Images," *IEEE Transactions on Geoscience and Remote Sensing*, 2024.
- [58] K. Jiang, W. Liu, Z. Wang, X. Zhong, J. Jiang, and C.-W. Lin, "DAWN: Direction-aware Attention Wavelet Network for Image Deraining," in *Proceedings of the 31st ACM International Conference on Multimedia*, ser. MM '23. New York, NY, USA: Association for Computing Machinery, 2023, p. 7065–7074.
- [59] K. Jiang, J. Jiang, X. Liu, X. Xu, and X. Ma, "FMRNet: Image Deraining via Frequency Mutual Revision," *Proceedings of the AAAI Conference on Artificial Intelligence*, vol. 38, no. 11, pp. 12 892–12 900, Mar. 2024.
- [60] Y. Xiao, Q. Yuan, K. Jiang, Y. Chen, Q. Zhang, and C.-W. Lin, "Frequency-Assisted Mamba for Remote Sensing Image Super-Resolution," 2024.
- [61] D. Hong, B. Zhang, X. Li, Y. Li, C. Li, J. Yao, N. Yokoya, H. Li, P. Ghamisi, X. Jia, A. Plaza, P. Gamba, J. A. Benediktsson, and J. Chanussot, "SpectralGPT: Spectral Remote Sensing Foundation Model," *IEEE Transactions on Pattern Analysis and Machine Intelligence*, vol. 46, no. 8, pp. 5227–5244, 2024.
- [62] C. Li, B. Zhang, D. Hong, J. Yao, and J. Chanussot, "LRR-Net: An Interpretable Deep Unfolding Network for Hyperspectral Anomaly Detection," *IEEE Transactions on Geoscience and Remote Sensing*, vol. 61, pp. 1–12, 2023.
- [63] C. Li, B. Zhang, D. Hong, J. Zhou, G. Vivone, S. Li, and J. Chanussot, "CasFormer: Cascaded transformers for fusion-aware computational hyperspectral imaging," *Information Fusion*, vol. 108, p. 102408, 2024.